Hybrid plasmonic lattices with tunable magneto-optical activity

Mikko Kataja,[1] Sara Pourjamal,[1] Nicolò Maccaferri,[2] Paolo Vavassori,[2,3] Tommi K. Hakala,[4] Mikko J. Huttunen,[4] Päivi Törmä,[4] and Sebastiaan van Dijken[1,*]

[1]NanoSpin, Department of Applied Physics, Aalto University School of Science, P.O. Box, 15100, FI-00076 Aalto, Finland
[2]CIC nanoGUNE, 20018 Donostia-San Sebastian, Spain
[3]IKERBASQUE, Basque Foundation for Science, 48011 Bilbao, Spain
[4]COMP Centre of Excellence, Department of Applied Physics, Aalto University, FI-00076 Aalto, Finland
[*]sebastiaan.van.dijken@aalto.fi

Abstract: We report on the optical and magneto-optical response of hybrid plasmonic lattices that consist of pure nickel and gold nanoparticles in a checkerboard arrangement. Diffractive far-field coupling between the individual emitters of the lattices results in the excitation of two orthogonal surface lattice resonance modes. Local analyses of the radiation fields indicate that both the nickel and gold nanoparticles contribute to these collective resonances and, thereby, to the magneto-optical activity of the hybrid arrays. The strong effect of noble metal nanoparticles on the magneto-optical response of hybrid lattices opens up new avenues for the realization of sensitive and tunable magneto-plasmonic nanostructures.

References and links

1. G. Armelles and A. Dmitriev, "Focus on magnetoplasmonics," New J. Phys. **16**(4), 045012 (2014).
2. G. Armelles, A. Cebollada, A. García-Martín, and M. U. González, "Magnetoplasmonics: combining magnetic and plasmonic functionalities," Adv. Opt. Mater. **1**(1), 10–35 (2013).
3. V. I. Safarov, V. A. Kosobukin, C. Hermann, G. Lampel, J. Peretti, and C. Marlière, "Magneto-optical effects enhanced by surface plasmons in metallic multilayer films," Phys. Rev. Lett. **73**(26), 3584–3587 (1994).
4. J. Ferré, G. Pénissard, C. Marlière, D. Renard, P. Beauvillain, and J. P. Renard, "Magneto-optical studies of Co/Au ultrathin metallic films," Appl. Phys. Lett. **56**(16), 1588–1590 (1990).
5. E. Ferreiro-Vila, J. B. González-Díaz, R. Fermento, M. U. González, A. García-Martín, J. M. García-Martín, A. Cebollada, G. Armelles, D. Meneses-Rodríguez, and E. M. Sandoval, "Intertwined magneto-optical and plasmonic effects in Ag/Co/Ag layered structures," Phys. Rev. B **80**(12), 125132 (2009).
6. G. Armelles, J. B. González-Díaz, A. García-Martín, J. M. García-Martín, A. Cebollada, M. Ujué González, S. Acimovic, J. Cesario, R. Quidant, and G. Badenes, "Localized surface plasmon resonance effects on the magneto-optical activity of continuous Au/Co/Au trilayers," Opt. Express **16**(20), 16104–16112 (2008).
7. J. B. González-Díaz, A. García-Martín, J. M. García-Martín, A. Cebollada, G. Armelles, B. Sepúlveda, Y. Alaverdyan, and M. Käll, "Plasmonic Au/Co/Au nanosandwiches with enhanced magneto-optical activity," Small **4**(2), 202–205 (2008).
8. J. C. Banthí, D. Meneses-Rodríguez, F. García, M. U. González, A. García-Martín, A. Cebollada, and G. Armelles, "High magneto-optical activity and low optical losses in metal-dielectric Au/Co/Au-SiO₂ magnetoplasmonic nanodisks," Adv. Mater. **24**(10), OP36–OP41 (2012).
9. R. Fujikawa, A. V. Baryshev, J. Kim, H. Uchida, and M. Inoue, "Contribution of the surface plasmon resonance to optical and magneto-optical properties of a Bi:YIG-Au nanostructure," J. Appl. Phys. **103**, 07D301 (2008).
10. S. Tomita, T. Kato, S. Tsunashima, S. Iwata, M. Fujii, and S. Hayashi, "Magneto-optical Kerr effects of yttrium-iron garnet thin films incorporating gold nanoparticles," Phys. Rev. Lett. **96**(16), 167402 (2006).
11. V. I. Belotelov, I. A. Akimov, M. Pohl, V. A. Kotov, S. Kasture, A. S. Vengurlekar, A. V. Gopal, D. R. Yakovlev, A. K. Zvezdin, and M. Bayer, "Enhanced magneto-optical effects in magnetoplasmonic crystals," Nat. Nanotechnol. **6**(6), 370–376 (2011).
12. N. de Sousa, L. S. Froufe-Pérez, G. Armelles, A. Cebollada, M. U. González, F. García, D. Meneses-Rodríguez, and A. García-Martín, "Interaction effects on the magneto-optical response of magnetoplasmonic dimers," Phys. Rev. B **89**(20), 205419 (2014).
13. G. Armelles, A. Cebollada, A. García-Martín, M. U. González, F. García, D. Meneses-Rodríguez, N. de Sousa, and L. S. Froufe-Pérez, "Mimicking electromagnetically induced transparency in the magneto-optical activity of magnetoplasmonic nanoresonators," Opt. Express **21**(22), 27356–27370 (2013).

14. V. Bonanni, S. Bonetti, T. Pakizeh, Z. Pirzadeh, J. Chen, J. Nogués, P. Vavassori, R. Hillenbrand, J. Åkerman, and A. Dmitriev, "Designer magnetoplasmonics with nickel nanoferromagnets," Nano Lett. **11**(12), 5333–5338 (2011).
15. J. Chen, P. Albella, Z. Pirzadeh, P. Alonso-González, F. Huth, S. Bonetti, V. Bonanni, J. Åkerman, J. Nogués, P. Vavassori, A. Dmitriev, J. Aizpurua, and R. Hillenbrand, "Plasmonic nickel nanoantennas," Small **7**(16), 2341–2347 (2011).
16. N. Maccaferri, J. B. González-Díaz, S. Bonetti, A. Berger, M. Kataja, S. van Dijken, J. Nogués, V. Bonanni, Z. Pirzadeh, A. Dmitriev, J. Åkerman, and P. Vavassori, "Polarizability and magnetoplasmonic properties of magnetic general nanoellipsoids," Opt. Express **21**(8), 9875–9889 (2013).
17. N. Maccaferri, A. Berger, S. Bonetti, V. Bonanni, M. Kataja, Q. H. Qin, S. van Dijken, Z. Pirzadeh, A. Dmitriev, J. Nogués, J. Åkerman, and P. Vavassori, "Tuning the magneto-optical response of nanosize ferromagnetic Ni disks using the phase of localized plasmons," Phys. Rev. Lett. **111**(16), 167401 (2013).
18. M. Kataja, T. K. Hakala, A. Julku, M. J. Huttunen, S. van Dijken, and P. Törmä, "Surface lattice resonances and magneto-optical response in magnetic nanoparticle arrays," Nat. Commun. **6**, 7072 (2015).
19. A. D. Humphrey and W. L. Barnes, "Plasmonic surface lattice resonances on arrays of different lattice symmetry," Phys. Rev. B **90**(7), 075404 (2014).
20. S. Zou and G. C. Schatz, "Silver nanoparticle array structures that produce giant enhancements in electromagnetic fields," Chem. Phys. Lett. **403**(1-3), 62–67 (2005).
21. V. G. Kravets, F. Schedin, and A. N. Grigorenko, "Extremely narrow plasmon resonances based on diffraction coupling of localized plasmons in arrays of metallic nanoparticles," Phys. Rev. Lett. **101**(8), 087403 (2008).
22. B. Auguié and W. L. Barnes, "Collective resonances in gold nanoparticle arrays," Phys. Rev. Lett. **101**(14), 143902 (2008).
23. Y. Chu, E. Schonbrun, T. Yang, and K. B. Crozier, "Experimental observation of narrow surface plasmon resonances in gold nanoparticle arrays," Appl. Phys. Lett. **93**(18), 181108 (2008).
24. N. Maccaferri, K. E. Gregorczyk, T. V. A. G. de Oliveira, M. Kataja, S. van Dijken, Z. Pirzadeh, A. Dmitriev, J. Åkerman, M. Knez, and P. Vavassori, "Ultrasensitive and label-free molecular-level detection enabled by light phase control in magnetoplasmonic nanoantennas," Nat. Commun. **6**, 6150 (2015).
25. F. Pineider, G. Campo, V. Bonanni, C. de Julián Fernández, G. Mattei, A. Caneschi, D. Gatteschi, and C. Sangregorio, "Circular magnetoplasmonic modes in gold nanoparticles," Nano Lett. **13**(10), 4785–4789 (2013).
26. B. Sepúlveda, J. B. González-Díaz, A. García-Martín, L. M. Lechuga, and G. Armelles, "Plasmon-induced magneto-optical activity in nanosized gold disks," Phys. Rev. Lett. **104**(14), 147401 (2010).
27. G. S. Krinchik and V. A. Artemev, "Magneto-optical properties of Ni, Co and Fe in the ultraviolet, visible and infrared parts of the spectrum," Sov. Phys. JETP **26**, 1080 (1986).
28. P. B. Johnson and R. W. Christy, "Optical constants of the noble metals," Phys. Rev. B **6**(12), 4370–4379 (1972).
29. S. Polisetty, J. Scheffler, S. Sahoo, Y. Wang, T. Mukherjee, X. He, and Ch. Binek, "Optimization of magneto-optical Kerr setup: analyzing experimental assemblies using Jones matrix formalism," Rev. Sci. Instrum. **79**(5), 055107 (2008).
30. A. Penttilä, E. Zubko, K. Lumme, K. Muinonen, M. A. Yurkin, B. Draine, J. Rahola, A. G. Hoekstra, and Y. Shkuratov, "Comparison between discrete dipole implementations and exact techniques," J. Quant. Spectrosc. Radiat. Transf. **106**(1-3), 417–436 (2007).
31. M. Meier and A. Wokaun, "Enhanced fields on large metal particles: dynamic depolarization," Opt. Lett. **8**(11), 581–583 (1983).
32. M. Meier, P. F. Liao, and A. Wokaun, "Enhanced fields on rough surfaces: Dipolar interactions among particles of sizes exceeding the Rayleigh limit," J. Opt. Soc. Am. B **2**(6), 931–949 (1985).
33. B. T. Draine and P. J. Flatau, "Discrete-dipole approximation for scattering calculations," J. Opt. Soc. Am. A **11**(4), 1491–1499 (1994).

1. Introduction

Combining strong local enhancements of electromagnetic fields in surface plasmon excitations with magneto-optically active ferromagnetic materials enables plasmonic structures that can be controlled by external magnetic fields. In particular, hybrid structures comprising noble metals and ferromagnetic metals or transparent magnetic garnets have been explored as plasmonic systems with integrated magneto-optical activity [1,2]. Examples include noble metal-ferromagnetic multilayers [3–6], metallic sandwich-structure nanodisks [7,8] and magnetic garnet films with integrated noble metal nanoparticles [9,10] or gratings [11]. In all these realizations, the magnetic constituent is in direct contact with the noble metal. Dimer nanodisks wherein a dielectric layer separates ferromagnetic and noble metal components have also been studied [8,12,13]. The close proximity of magneto-optically active and non-active elements in a single nanodisk can induce magneto-optical activity on the non-magnetic metal via near-field dipole-dipole interactions if the thickness of the dielectric is small (<50 nm in [13]).

In addition to the hybrid structures discussed above, pure ferromagnetic nanoparticles also support the excitation of localized surface plasmon resonances (LSPRs) [14–17]. While the optical response of individual ferromagnetic nanoparticles is limited by ohmic losses, the arrangement of such particles in periodic arrays can enhance the optical and magneto-optical activity by the excitation of surface lattice resonances (SLRs) [18]. This effect, which arises from coupling between broad LSPRs and the diffracted orders of the lattice [19–23], can produce sharp and asymmetrical resonances in optical and magneto-optical spectra of ferromagnetic nanoparticle arrays. Diffractive coupling between nanoscale emitters in periodic arrays is of the far-field type and, consequently, it is not limited to short distances.

Here, we explore nanoparticle arrays with an ordered checkerboard pattern of ferromagnetic (nickel) and noble metal (gold) emitters that are physically separated by a distance of 450 nm. The gold constituent of these arrays guarantees an intense optical activity as demonstrated by high reflectivity. Yet, compared to pure nickel nanoparticle arrays, the magneto-optically induced orthogonal SLR mode retains its intensity. Our experimental results are explained by far-field diffractive coupling between the two types of nanoparticles which (1) induces magneto-optical activity on the gold particles and (2) enhances the magneto-optical signal of the nickel particles, findings that are substantiated by numerical simulation. In addition, we show that the optical and magneto-optical response of the hybrid arrays can be tailored by varying the size of the non-magnetic gold nanoparticles. The proven ability to enhance optical responses while conserving intense magneto-optical activity can be used to accurately measure very small refractive index changes in label-free biosensing applications [24].
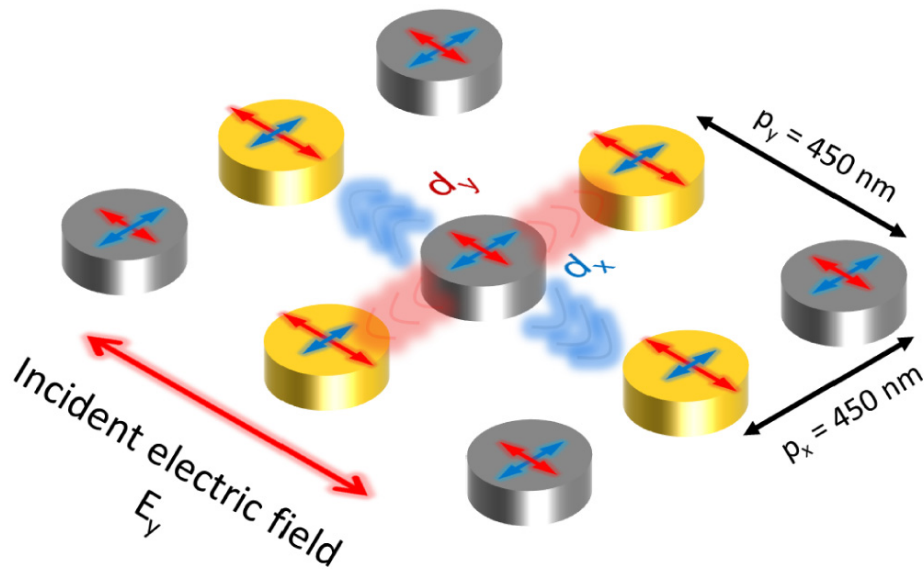

Fig. 1. Schematic illustration of a checkerboard array of nickel (gray) and gold (yellow) nanoparticles. In the experiments, normal incident light with linear polarization along the y-axis is used to characterize the optical and magneto-optical response while the magnetization of the nickel particles is oriented out-of-plane by a magnetic field. The arrows illustrate the electric dipoles in the nanoparticles that are directly induced by the external electric field (optical dipoles in red), excited by spin-orbit coupling in the nickel nanoparticles (magneto-optical dipoles in blue), and induced in the gold nanoparticles via far-field diffractive coupling to nickel particles (magneto-optical dipoles also in blue). The dipoles couple primarily along the x- and y-directions of the lattice.

2. Experimental results

Nanoparticle arrays of three different material compositions were fabricated on glass substrates using electron-beam lithography, namely pure nickel, pure gold and hybrid arrays with nickel and gold particles arranged in a checkerboard pattern. A double exposure technique was used for the hybrid particle arrays. First, Au nanoparticles and alignment marks were patterned by electron-beam exposure of a first PMMA resist layer and lift-off. A second PMMA layer was subsequently spin-coated. Before exposing this layer, the nickel pattern was carefully aligned to the gold particles. The hybrid array was completed by electron-beam evaporation of a nickel film and lift-off. The diameter of the nickel particles was 120 nm in all arrays while the diameter of the gold particles was varied from 80 to 120 nm to examine tuning of the magneto-optical response by narrow LSPRs in the gold particles. The thickness of all particles was 30 nm and the lattice period of the square arrays was fixed at p = 450 nm. To confirm that the observed effects truly originate from the periodic arrangement of nickel and gold nanoparticles, samples with random distributions of the same particles were also fabricated and analyzed. The samples were immersed in refractive index matching oil (n = 1.51) to provide a symmetric refractive index environment in all measurements.

Figure 1 illustrates the geometry of the experimental system. An external electric field E_y induces a dipole moment d_y in each nanoparticle that radiates predominantly along the x-axis. For normal incident light, the radiation fields from all particles interfere constructively at $p = \lambda/n$, where λ is the free space wavelength of the incident radiation and n is the refractive index of the medium surrounding the particles.

For magneto-optically active materials, the induced dipole moments interact with the magnetization of the nanoparticles giving rise to Kerr (reflection) and Faraday (transmission) effects. In this study, we explore the polar magneto-optical Kerr effect (P-MOKE) for nickel nanoparticles with saturated out-of-plane magnetization. Upon reflection from the magnetized sample, the linear polarization of the incident light rotates and it becomes elliptical. The magneto-optical response of an isolated ferromagnetic nanoparticle can be conveniently understood as an excitation of two orthogonal dipole moments, the first, d_y, arising from direct excitation by the external electric field, and the second, d_x, induced by intrinsic spin-orbit coupling [17]. For the typical case $|d_y| \gg |d_x|$, the magneto-optical Kerr rotation θ and Kerr ellipticity ε are defined as $\theta = \mathrm{Re}(d_x/d_y)$ and $\varepsilon = \mathrm{Im}(d_x/d_y)$, and the magnitude of the complex magneto-optical Kerr angle is given by $\Phi = \sqrt{\theta^2 + \varepsilon^2}$ = $|d_x|/|d_y|$. Hereafter we will refer to d_y and d_x as optical and magneto-optical dipoles, respectively. An analytical expression for the magneto-optical response of a periodic array of ferromagnetic nanoparticles is given in [18].

Optical and magneto-optical measurements were performed in reflection geometry at normal incidence (angle of incidence <0.4°). In this configuration, the reflected intensity is approximately proportional to the modulus squared of the directly excited dipoles, i.e. $|d_y|^2$. In both optical and magneto-optical measurements, reflections from the back side of the glass substrate were eliminated by placing a wedge prism behind the substrate to deflect the transmitted beam. The reflection from the front of the cover glass was measured separately and subtracted from the measurement data. The magneto-optical measurements were carried out by measuring full hysteresis loops for each wavelength in out-of-plane magnetic fields up to ± 400 mT, which was sufficient to fully saturate the magnetization of the nickel nanoparticles. The values for the magneto-optical Kerr rotation and Kerr ellipticity were determined from the hysteresis loops by averaging the magneto-optical signal in saturation after subtraction of any linear contributions. Possible effects arising from diamagnetism in the gold nanoparticles or the glass substrate are thus eliminated from the measurement data [25,26]. More details on the experimental setup and measurement procedure are given in Appendix A.
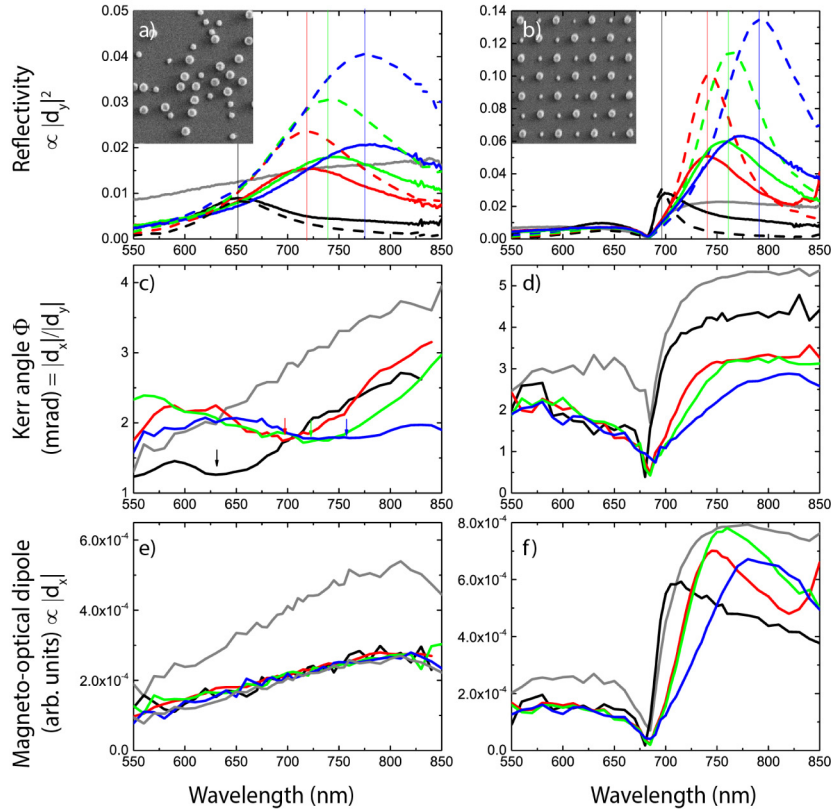
Fig. 2. Experimental results. (a) Optical reflectivity of randomly distributed nanoparticles. Solid gray line: nickel (particle diameter d_{Ni} = 120 nm). Dashed lines: gold (particle diameter d_{Au} = 80 nm (black), 100 nm (red), 110 nm (green), 120 nm (blue)). Other solid lines: mixture of nickel and gold nanoparticles (d_{Au} = 80 nm (black), 100 nm (red), 110 nm (green), 120 nm (blue), d_{Ni} = 120 nm). The particle density is the same for all samples. Inset: SEM micrograph of a sample with randomly distributed nickel (d_{Ni} = 120 nm) and gold (d_{Au} = 100 nm) nanoparticles. (b) Optical reflectivity of nanoparticle arrays (p = 450 nm). Solid gray line: nickel (d_{Ni} = 120 nm). Dashed lines: gold (d_{Au} = 80 nm (black), 100 nm (red), 110 nm (green), 120 nm (blue)). Other solid lines: nickel and gold nanoparticles in a checkerboard pattern (d_{Au} = 80 nm (black), 100 nm (red), 110 nm (green), 120 nm (blue), d_{Ni} = 120 nm) Inset: SEM micrograph of a checkerboard array of nickel (d_{Ni} = 120 nm) and gold (d_{Au} = 80 nm) nanoparticles. (c),(d) Magneto-optical Kerr angle of randomly distributed nanoparticles (c) and periodic particle arrays (d) (same labeling as in (a) and (b)). (e),(f) Magneto-optical dipole signal for randomly distributed nanoparticles (e) and periodic particle arrays (f). The curves in (e) and (f) are obtained by multiplying the magneto-optical Kerr angle ((c) and (d)) and the square root of the optical reflectivity ((a) and (b)).

Figure 2 shows the optical reflectivity of the nickel, gold and mixed samples with random and periodic particle arrangements. The reflectivity maxima of the randomly distributed gold nanoparticles are caused by the excitation of LSPRs, as illustrated by the characteristic redshift with increasing particle diameter. Replacing half of the gold nanoparticles with nickel reduces the reflectivity of the samples by about 50%, yet spectral shifts of the resonance condition are not observed. The gold LSPRs thus fully dominate the optical spectrum of randomly distributed gold and nickel particles and contributions from the relatively weak plasmon excitations in the nickel nanoparticles are negligible. In contrast, the optical properties of periodic nanoparticle arrays depend strongly on both the noble metal and ferromagnetic constituents of the lattice, as illustrated by the optical reflectivity spectra in Fig. 2(b). In all cases (pure nickel, pure gold, and mixed arrays), Fano-type SLRs arising from coupling between the narrow lattice resonance at $\lambda = n \times p$ = 688 nm (Rayleigh anomaly) and

broader LSPRs are observed. The intensity of the reflectivity maxima is largest for the pure gold samples and it is considerably reduced for the nickel nanoparticle array. The reflectivity spectra of the nickel-gold checkerboard patterns fall between these two limiting cases due to stronger damping in the nickel nanoparticles. Interestingly, the reflectivity maxima of the mixed arrays are blue-shifted when compared to the pure gold samples, as illustrated by the vertical lines in Fig. 2(b). This observation indicates that the nickel particles play an active role in the emergence of the SLR modes of the mixed systems, that is, their role is not merely limited to the introduction of damping. This conclusion is further supported by the wavelength of the Rayleigh anomaly, which is identical for all lattices irrespective of composition.

The magneto-optical Kerr spectra of samples with random distributions of nickel nanoparticles and nickel-gold nanoparticle mixtures are shown in Fig. 2(c). The magneto-optical activity of random nickel nanoparticles monotonically increases with the wavelength of incident radiation because of a growing magneto-optical coupling strength (Voigt parameter Q) in this wavelength range [27]. In contrast, non-monotonic line shapes with a characteristic minimum are measured on the mixed samples. The minima in the Kerr spectra of Fig. 2(c) closely coincide with maxima of the optical reflectivity curves in Fig. 2(a). Variation of the magneto-optical Kerr angle, i.e. $|d_x|/|d_y|$, can therefore be attributed to the excitation of more intense optical dipoles d_y in the gold nanoparticles. This observation is further illustrated by plots of the magneto-optical dipole signal in Fig. 2(e), which are obtained by multiplying the Kerr angle of Fig. 2(c) with the square root of the optical reflectivity in Fig. 2(a). The signal, which is proportional to the magnitude of d_x in the nickel nanoparticles, is identical for all nickel-gold mixtures and it is reduced by half compared to that of the pure nickel sample. In other words, the decrease of the magneto-optical dipole signal is simply caused by substitution of half of the nickel nanoparticles with non-magnetic gold, while more intense d_y's in the gold nanoparticles reduce the Kerr angle when gold LSPRs are excited.

In periodic arrays of ferromagnetic nanoparticles, magneto-optical dipoles d_x can couple to the diffracted orders of the lattice along the y-axis, leading to Fano-type SLRs in the magneto-optical Kerr spectra [18]. Figure 2(d) reveals that diffractive far-field coupling along the y-axis of the arrays is also effective for nickel-gold checkerboard lattices despite the fact that neither isolated nor arrays of gold nanoparticles display any magneto-optical activity on their own. The asymmetric Kerr spectra of the arrays are characterized by a minimum at the (0,1) diffracted order (Rayleigh anomaly at 688 nm), which is followed by a strong and steep increase of the magneto-optical Kerr angle with increasing wavelength. The largest signal is obtained for pure nickel, while it is found to decrease with the diameter of the gold nanoparticles for nickel-gold checkerboard arrays. The latter dependence is predominantly caused by the excitation of more intense optical dipoles (i.e. increase of $|d_y|$) in the gold nanoparticles, which decreases the Kerr angle $|d_x|/|d_y|$ of the entire sample.

To isolate the effect of magneto-optical dipoles d_x and coupling of these LSPR modes along the y-axis of the nanoparticle lattice, we again multiply the Kerr angle by the square root of the optical reflectivity. The resulting spectra in Fig. 2(f) show some striking features. First, contrary to randomly distributed nickel and gold nanoparticles, we find that the magneto-optical dipole signal of nickel-gold checkerboard arrays depends on the size of the gold particles. Second, the magnitude of the signal is not just reduced by half compared to that of the pure nickel sample, but it strongly varies with the wavelength of the incoming light. Maxima of the curves in Fig. 2(f) occur at wavelengths that coincide with strong optical reflection. This signifies that coupling between LSPRs and the diffracted orders of the hybrid lattices enhances both the optical reflectivity ($\propto |d_y|^2$) and the magnitude of the magneto-optically induced collective SLR mode ($\propto |d_x|$). For the mixed array with 110 nm gold particles, for example, the maximum magnitude of d_x is nearly identical to that of the pure nickel sample near the resonance condition, yet its spectral features are considerably sharper. All these effects can only be rationalized if the gold nanoparticles significantly contribute to the coupling of magneto-optical dipoles along the y-axis of the periodic lattice.

3. Model calculations and simulations

To further elucidate the active role of gold nanoparticles in the magneto-optical response of gold-nickel checkerboard arrays, we performed numerical calculations using the discrete dipole approximation (DDA). The polarizability of single nickel and gold nanoparticles were calculated using the approach of [16] with measured permittivities of nickel and gold as input parameters [27,28]. Magneto-optical effects were introduced in the DDA model via off-diagonal elements in the nickel polarizability tensor only (i.e. the gold nanoparticles were assumed to have zero intrinsic magneto-optical activity). The particle arrays were surrounded by a homogeneous medium with refractive index $n = 1.51$ and normal incident plane waves with linear polarization along the y-axis were used for excitation (see Appendix B for more details).
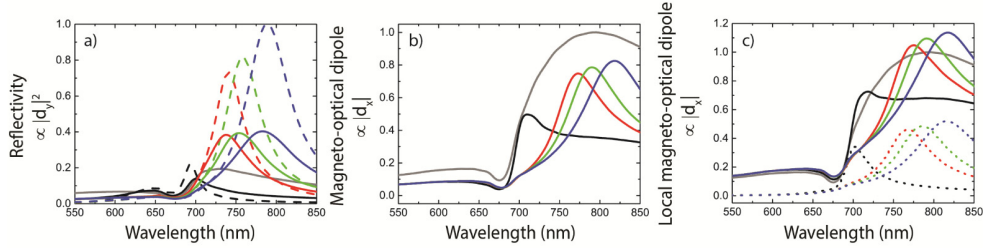

Fig. 3. DDA model calculations. (a) Optical reflectivity of pure nickel, pure gold, and mixed nickel-gold nanoparticle arrays ($p = 450$ nm), normalized to the maximum signal of a pure gold array with $d_{Au} = 120$ nm. Solid gray line: nickel ($d_{Ni} = 120$ nm). Dashed lines: gold ($d_{Au} = 80$ nm (black), 100 nm (red), 110 nm (green), 120 nm (blue)). Other solid lines: nickel and gold nanoparticles in a checkerboard pattern ($d_{Au} = 80$ nm (black), 100 nm (red), 110 nm (green), 120 nm (blue), $d_{Ni} = 120$ nm). (b) Magneto-optical dipole strength for pure nickel and mixed nickel-gold arrays. The curves in (b) represent the response of full arrays, which is proportional to the sum of magneto-optical dipoles d_x in the nickel and gold nanoparticles. (c) Magnitude of individual dipoles d_x in nickel (solid lines) and gold (dotted lines) nanoparticles for pure nickel and mixed nickel-gold arrays. The color labels in (b) and (c) are the same as in (a) and the calculations are normalized to the maximum dipole strength in the pure nickel array.

Figure 3(a) shows DDA calculations of the optical reflectivity for periodic arrays with only nickel (solid gray line), only gold (dashed lines), and a checkerboard pattern of nickel and gold (other solid lines) nanoparticles. The numerical results reproduce the main features of the experimental reflectivity spectra in Fig. 2(b). In particular, the model calculations confirm that the insertion of gold nanoparticles in a nickel lattice considerably enhances the optical reflectivity via a reduction of the Fano-type SLR line width.

The average strength of electric dipoles along the x-axis of pure nickel and hybrid nickel-gold nanoparticle arrays is shown in Fig. 3(b). DDA calculations show that the replacement of every second nickel particle with gold does not just reduce the spin-orbit induced dipole signal by half. The reason for this is twofold, as clearly illustrated by plots of the individual dipole strength $|d_x|$ in the nickel and gold particles of the checkerboard patterns in Fig. 3(c). First, diffractive far-field coupling between the nickel and gold nanoparticles along the y-axis of the array induces a considerable orthogonal dipole d_x on the latter. As a consequence, the gold particles contribute to the magneto-optical activity of the hybrid array. For all lattices, the strength of d_x in the gold particles is almost half the magnitude of d_x in nickel. Second, the magnitude of d_x in nickel is sustained by coupling to strong d_y's in gold (along the x-axis), which reduces the spectral linewidth of the d_y's and d_x's in nickel (the latter via intrinsic spin-orbit interactions within the nickel particles). In fact, for $d_{Au} = 100$ nm, 110 nm, and 120 nm, the maximum magneto-optical dipole strength in nickel is somewhat larger for the mixed array than for the pure nickel lattice and the width of the resonance peak is reduced by a factor $3 – 4$ (compare gray and colored lines in Fig. 3(c)). Besides the size of the gold nanoparticles, the optical and magneto-optical signals of hybrid arrays also depend on other

parameters. Most notably, these include the size of the nickel particles, the shape of the particles, the distribution of nickel and gold particles within the lattice, and the geometry of the array. The strong dependence of magneto-optical spectra on the noble metal constituent of hybrid nanoparticle arrays and geometry open up avenues for the design of tailored magneto-optical responses.
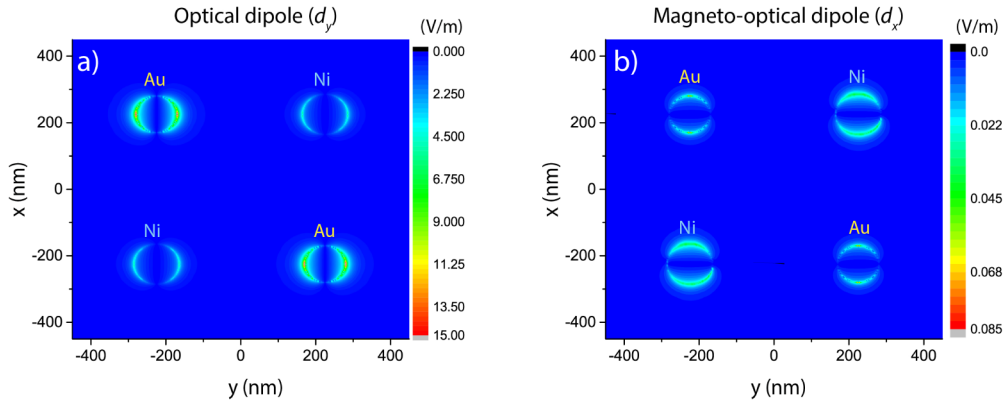

Fig. 4. (a) Electric field intensity distribution in a checkerboard array of nickel (d_{Ni} = 120 nm) and gold (d_{Au} = 110 nm) nanoparticles for λ = 750 nm. (b) Magneto-optical dipoles in the same array.

Finally, we discuss the distribution of electric fields inside the nanoparticles of a checkerboard array as numerically simulated using the finite-difference time-domain (FDTD) method. In the simulations, a unit cell of two nickel (d_{Ni} = 120 nm) and two gold (d_{Au} = 110 nm) nanoparticles was used and periodic boundary conditions were applied to mimic a large periodic array. The wavelength of incident radiation was set to λ = 750 nm, because both optical and magneto-optical responses are strong under this condition. Spin-orbit interactions in the nickel nanoparticles were introduced in the FDTD simulations via off-diagonal terms in the nickel dielectric tensor. More details on the FDTD simulations are provided in Appendix C.

The electric field distribution profile of the array is shown in Fig. 4(a). The intensity maxima along the y-axis of the nanoparticles reflect direct dipolar excitations by the incident radiation, which are stronger in the gold particles. The weaker magneto-optical dipoles along the x-axis of the particles are present but not visible. To visualize the orthogonal dipoles, we eliminated the direct excitations by subtracting simulation results for arrays wherein the perpendicular magnetization of the nickel nanoparticles is saturated along the up and down directions. The result is shown Fig. 4(b). The electric fields that are produced by intrinsic spin-orbit interactions in nickel and via diffractive far-field coupling in gold, have similar distribution profiles as the optical dipoles. The electric field intensity in Fig. 4(b) is largest in the nickel nanoparticles, yet considerable magneto-optical dipoles are also excited in gold. The DDA calculations and FDTD simulations in Figs. 3 and 4 thus both corroborate the experimental observations of Fig. 2 that the magneto-optical response of hybrid particle arrays is governed by collective modes involving optical and magneto-optical plasmon excitations in both the nickel and gold nanoparticles. Diffractive far-field coupling between magnetic and noble metal particles leads to the conservation of strong magneto-optical signals while significantly enhancing the optical reflectivity compared to pure nickel particle arrays. This ability to independently tailor optical and magneto-optical responses in hybrid plasmonic material systems is particularly attractive for sensor applications.

4. Conclusions

In summary, we have demonstrated a novel method for integrating magneto-optically active elements into plasmonic nanostructures. It was shown that checkerboard arrays of nickel and

gold nanoparticles combine intense optical resonances with strong magneto-optical activity. Experimental comparisons with random particle distributions and numerical simulations of periodic lattices indicate that the effects are caused by diffractive far-field coupling between the magnetic and noble metal components of the hybrid lattice. Since the underlying interaction mechanisms are generally applicable, we anticipate that our results will stimulate work on other mixed particle configurations such as rectangular and hexagonal lattices.

Appendix A - Optical and magneto-optical measurements

Optical reflectivity and magneto-optical Kerr effect measurements were conducted with a Kerr spectrometer as schematically shown in Fig. 5. The setup consisted of a broadband supercontinuum laser (NKT SuperK EXW-12 with acousto-optical filter), polarizing (Glann-Thompson prism, CVI MellesGriot) and focusing optics, a photoelastic modulator (Hinds Instruments I/FS50), and a photodetector. The wavelength of the laser was tuned between 550 nm and 850 nm. The angle of incidence with respect to the surface normal was <0.4° and an electromagnet (GMW 3470) was used to reorient the magnetization of the Ni nanoparticles between the two out-of-plane directions in a field of ±400 mT. This corresponds to the polar magneto-optical Kerr effect (P-MOKE) geometry. The Kerr ellipticity and Kerr rotation were simultaneously recorded by lock-in amplification of the modulated signal at 50 kHz and 100 kHz. From the hysteresis curves, a small linear contribution was first subtracted to eliminate diamagnetic and Faraday effects. After this, the amplitude of the complex Kerr angle was calculated from the average signal in magnetic saturation using $\Phi = \sqrt{\theta^2 + \varepsilon^2}$. In all measurements, the samples were immersed in refractive index matching oil (n = 1.51) to provide a symmetric refractive index environment. Reflections from the back side of the glass substrate were eliminated by affixing a glass wedge prism (Thorlabs PS812) behind the substrate with index matching oil. The reflected intensity from the front cover glass was subtracted from the measurement signal. In the reflectivity measurements, the spectrum of the laser light was measured by placing a mirror next to the sample. A detailed Jones matrix description of the optical components in the setup is given in [29].
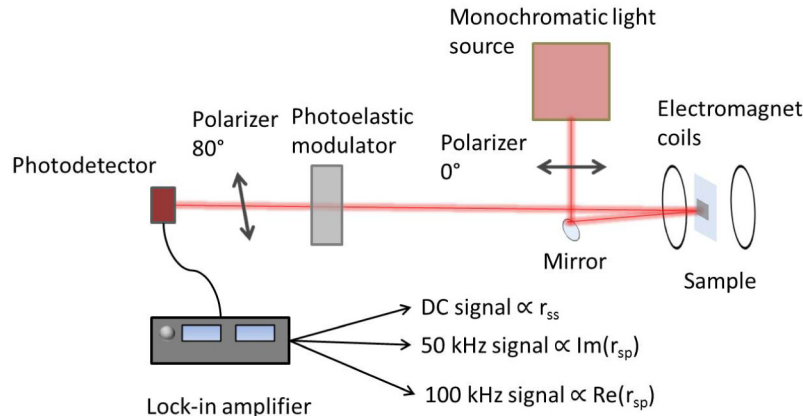

Fig. 5. Schematic illustration of the magneto-optical Kerr effect spectrometer.

Appendix B - DDA calculations

A discrete dipole approximation was used to model the optical and magneto-optical response of nanoparticle array [30]. The polarizabilities of the nickel and gold nanoparticles were calculated using a modified long wavelength approximation [31,32] where the magneto-optical properties of nickel were introduced via off-diagonal elements in the polarizability tensor of the nickel nanoparticles following the approach of [16] and no magneto-optical properties were included for the gold nanoparticles. Experimentally measured values were

used for the permittivity of gold and nickel [27,28]. The refractive index of the medium surrounding the nanoparticles was set to $n = 1.51$ and a plane wave with linear polarization was used for excitation.

The self-consistent internal field was solved using DDA. To obtain the scattered fields in the backward direction we used [33]:

$$E_{sca} = k^2 \frac{e^{ikr}}{r} \sum_{j=1}^{N} \left(\overline{I} - \hat{r}\hat{r} \right) \alpha \cdot E_{loc}$$

where k is the amplitude of the wave vector, $\overline{I}$ is the identity dyadic and $\hat{r}\hat{r}$ is the dyadic product of radial unit vector $\hat{r}$. Optical reflectivity spectra were calculated by taking the modulus squared of the scattered field. The spectral evolution of the magneto-optical dipole strength was obtained by plotting the induced polarization $P = \alpha E_{loc}$ along the orthogonal x-axis of the nanoparticles.
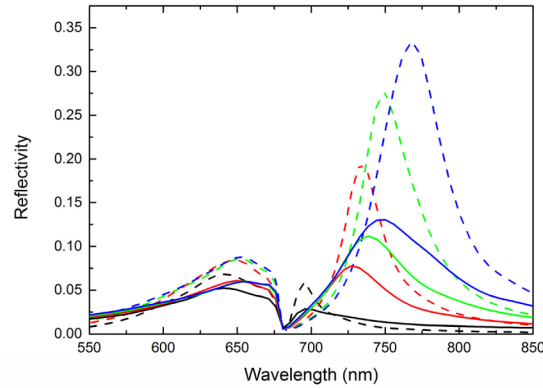
Appendix C - FDTD simulations

Fig. 6. FDTD optical reflectivity spectra for pure gold nanoparticle arrays (dashed lines) and nickel-gold checkerboard arrays (solid lines) with $p = 450$ nm. The diameters of the particles are $d_{Ni} = 120$ nm and $d_{Au} = 80$ nm (black), 100 nm (red), 110 nm (green), 120 nm (blue).

FDTD simulations were carried out using commercial FDTD Solutions software from Lumerical. A unit cell of two nickel and two gold nanoparticles in checkerboard geometry was simulated. The particles were placed in a 900×900 nm simulation area at coordinates $x = -225$, $y = -225$ and $x = 225$, $y = 225$ (nickel nanoparticles) and $x = -225$, $y = 225$ and $x = 225$, $y = -225$ (gold nanoparticles). The diameters of the particles were $d_{Ni} = 120$ nm and $d_{Au} = 110$ nm and the thickness of all particles was set to 30 nm. Linearly polarized light was assumed to impinge along the sample normal. Periodic boundary conditions were applied at the edges of the simulation area to produce electric field distributions that are representative for a large checkerboard array. As surrounding, a uniform embedding medium with a dielectric constant of $n = 1.5$ was used. A uniform 2.5×2.5×2.5 nm mesh around the nanoparticles and a non-uniform surrounding mesh over the entire simulation area was used to test for convergent results. Broadband reflectivity spectra were obtained by placing an electric field monitor 2 μm above the nanoparticles. The near-field distribution profiles in Fig. 4 were calculated for a wavelength where both optical and magneto-optical effects are strong ($\lambda = 750$ nm). The magneto-optical effects were introduced in the FDTD simulations via off-diagonal terms in the nickel dielectric tensor, while the gold disks were initiated with an isotropic dielectric function (zero intrinsic magneto-optical activity). The distribution of magneto-optical dipolar fields in Fig. 4(b) was obtained by subtracting simulation results for the magnetization of the nickel nanoparticles pointing up and down. In the simulations, these two magnetization configurations were implemented by using opposite signs for the off-diagonal terms in the

nickel dielectric tensor. The results were divided by a factor two to appropriately reflect the magneto-optical dipole strength. FDTD simulations were also used to calculate the optical reflectivity spectra for pure gold and nickel-gold checkerboard arrays. The results, which are shown in Fig. 6, qualitatively agree with the experimental data of Fig. 2(b).